WILEY

RESEARCH ARTICLE

Analysis of the Surface Urban Heat Island Effect and the Spatiotemporal Heterogeneity of Its Driving Factors

Xuqian Rao[1] | Haifu Cui[1] 🔟 | Jiaying Dong[1] | Longwei Xiang[1] | Li Peng[2]

[1]School of Geosciences, Yangtze University, Wuhan, China | [2]Jingzhou Natural Resources Satellite Application Technology Center, Jingzhou, China

Correspondence: Haifu Cui (cuihaifu@yangtzeu.edu.cn)

ABSTRACT

The surface urban heat island (SUHI) effect presents a significant challenge in urban environments. However, there is spatio-temporal variability in the SUHI effect and its drivers, which is often overlooked. To address this issue, this study employs the geographically and temporally weighted regression (GTWR) model to analyze the spatiotemporal heterogeneity of the SUHI and its driving factors. The findings reveal the following: (1) The SUHIs in the central urban area of Wuhan are located mainly on both sides of the Yangtze and Han Rivers, most notably in the Qingshan Industrial Zone; (2) in the city center, the land surface temperature (LST) is strongly positively correlated with the bare soil index (BSI), normalized difference built-up index (NDBI), normalized difference vegetation index (NDVI), and nighttime light (NTL); (3) clear temporal disparities exist between the LST and the drivers, with the NDBI, NDWI, and NTL factors displaying the most notable variations; and (4) a comprehensive analysis has yielded quantitative relationships between the LST and associated drivers. In summary, it has been proven that there are spatiotemporal differences in the LST and its driving factors. Therefore, the impact of spatiotemporal heterogeneity should be considered when studying the mitigation of the SUHI effect.

1 | Introduction

In recent years, with the acceleration of urbanization, many natural surfaces have been replaced by impervious materials with high heat capacities, such as concrete and asphalt (Nowak and Greenfield 2020; Weng et al. 2011; Zhao et al. 2020). Furthermore, the continuous growth of urban populations, along with the ongoing increase in industrialization and modernization levels, has generated a substantial amount of anthropogenic heat (Feng et al. 2023; Guo et al. 2022; Li et al. 2021; Mishra and Arya 2024; Wu et al. 2021; Zhao et al. 2016). The comprehensive effects of these factors exacerbate the formation of SUHI (Deilami et al. 2018; Ghanbari et al. 2023). The SUHI effect was first proposed by Howard, who reported relatively higher temperatures in urban areas than in the surrounding suburban/rural areas (Howard 1833). The SUHI effect not only impacts the local climate but also exerts a multifaceted influence on residents' lives. For example, high temperatures restrict daily activities, and extreme heat can potentially lead to heatstroke (Meng et al. 2020; Templeton and Taleghani 2024). Moreover, the SUHI effect can impede air circulation between urban and rural areas, hindering the dispersion of dust and harmful gases in cities, and thereby posing threats to the safety of residents' lives and property (Rees et al. 2024; Sagris and Sepp 2017; Soltani and Sharifi 2017). Therefore, the study of the SUHI effect holds significant value for improving the natural environment, enhancing residents' quality of life, and providing governments with informed references for rational urban planning.

The first SUHI observations that used remote sensing technology were reported by Rao, who reported that remote sensing images can enable spatially continuous analyses compared with the sparse coverage obtained by meteorological monitoring of SUHI effect (Rao 1972). Since then, a variety of sensor platforms using various methods have been applied. Current research has focused mainly on the spatiotemporal distribution patterns of SUHI and the analysis of their driving factors, with the primary objective of providing scientific references for policymaking to mitigate SUHI (Niu et al. 2022; Zhu et al. 2020; Guha and Govil 2023).

In studies on the driving factors of the SUHI, Min et al. and Li et al. employed Landsat thermal infrared band data to derive the LST. They conducted ordinary least squares (OLS) regression analyses with LST and found that both land configuration and human activities captured significant explanatory power for the SUHI (Li et al. 2016; Min et al. 2019). Liu et al. and Zhang et al. utilized MODIS LST products and employed a geodetector metric to explore the dominant drivers of SUHI, which included elevation, land use/land cover (LULC), the vegetation index, impervious surfaces, waterbody coverage, the gross domestic product (GDP), POP, and NTL (Liu et al. 2021; Zhang, Li, et al. 2023). Gao et al. and Zhao et al. utilized geographically weighted regression (GWR) to investigate the relationships between the SUHI and block morphology and biophysical attributes (Gao et al. 2022; Zhao et al. 2018). The aforementioned studies have identified significant heterogeneity between SUHI and their driving factors; however, they have focused primarily on spatial heterogeneity analyses (Chen et al. 2022; Liao et al. 2021; Si et al. 2023). Fewer studies have explored the temporal heterogeneity between the SUHI effect and its driving factors. The GTWR model is well suited for elucidating the spatiotemporal heterogeneity among variables (Chu et al. 2015; Fotheringham et al. 2015; Wang et al. 2022; Wu et al. 2024; Zhao et al. 2023). Therefore, building on existing research findings and employing the GTWR model, this paper focuses on the central urban area of Wuhan, Hubei Province, China. This study primarily analyzed the spatiotemporal heterogeneity in the relationships between the SUHI effect and its driving factors, providing a spatiotemporal analytical perspective to understand the mechanisms influencing the SUHI effect.

2 | Study Area Overview and Data Sources

2.1 | Study Area Overview

Wuhan (30°35′N to 31°15′N, 113°41′E to 115°05′E) is a major city in central China and serves as a hub for politics, economy, finance, culture, education, and transportation. It is situated in the eastern part of the Jianghan Plain at the confluence of the Yangtze and Han Rivers. The terrain is flat, with an average elevation of approximately 0.023 km above sea level. Its total area is approximately 8569.15 km², with a permanent population of 13.64 million in 2022. Wuhan is characterized by a subtropical humid monsoon climate with distinct seasons. The summer is hot and humid, the winter is cold and rainy, and the spring and autumn are mild and favorable. Owing to population growth and urban expansion in recent years, Wuhan has faced challenges associated with the SUHI effect and is renowned as one of China's four "furnace cities" (Chen et al. 2019; Gui et al. 2019; Huang and Wang 2019). Therefore, this study focuses on the central urban districts of Wuhan, including Jiang'an District, Jianghan District, Qiaokou District, Hanyang District, Wuchang District, Qingshan District, and Hongshan District (Figure 1).
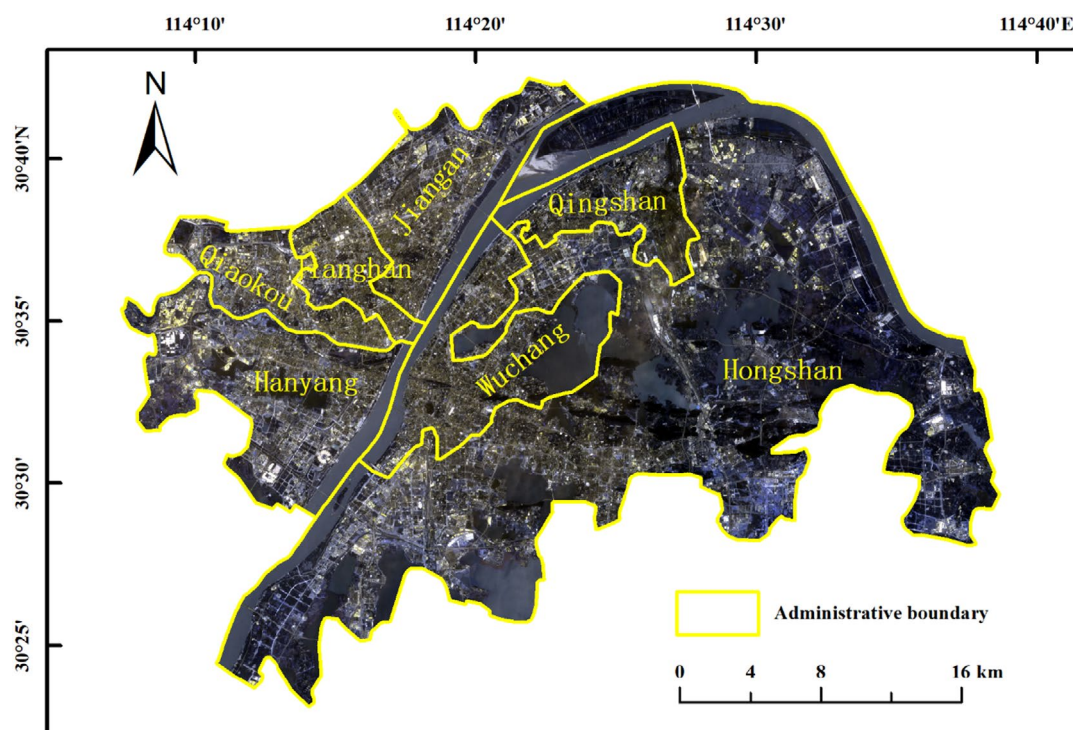

FIGURE 1 | Study area.

2.2 | Data Sources

This study utilized multisource data, including Landsat 8 satellite imagery with acquisition dates of July 31, 2013, September 15, 2018, and August 9, 2022, all during the summer season in Wuhan. The satellite overpass occurred at approximately 11 a.m. local time, and all images had cloud coverage of less than 5%, making them suitable for analyzing the SUHI. Additionally, population density data, VIIRS nighttime light data, and administrative boundary data from China were used in this study. The details of data type, resolution, and data source are presented in Table 1.

3 | Research Methods

3.1 | Land Surface Temperature Retrieval Method

In this study, the land surface temperature T_s was retrieved by employing an improved single-channel algorithm based on the 10th band of Landsat 8, as developed by Hu et al. (2015). The details of the algorithm are delineated as follows:

$$T_s = \frac{\left[K_2(\varphi_1 + \varphi_2)T_{10} + (1 - \varphi_1 - \varphi_2)T_{10}^2 - K_2\varphi_2 T_a\right]}{K_2\varphi_1} \quad (1)$$

In which,

$$\varphi_1 = \epsilon_{10}\tau_{10} \quad (2)$$

$$\varphi_2 = (1 - \tau_{10})\left[1 + (1 - \epsilon_{10})\tau_{10}\right] \quad (3)$$

$$T_{10} = \frac{K_2}{\ln\left(\frac{K_1}{L_{10}} + 1\right)} \quad (4)$$

$$T_a = 16.0110 + 0.92621T_0 \quad (5)$$

where K_1 and K_2 represent the radiometric calibration constants for Landsat 8's 10th band, which are accessible through the metadata of the remote sensing images. In this study, $K_1 = 774.89$, and $K_2 = 1321.08$. T_{10} represents the brightness temperature of the 10th band, and T_a represents the average atmospheric temperature, which was estimated via the midlatitude summer atmospheric model in this study (Qin et al. 2001). ϵ_{10} denotes the surface emissivity for the 10th band, derived from formulas (5–8).

TABLE 1 | Data sources.

Data types	Resolution	Data source
Landsat 8 OLI[a]	30 m	https://earthexplorer.usgs.gov/
Landsat 8 TIRS[a]	100 m	
Population data	1000 m	https://landscan.ornl.gov/
VIIRS	750 m	https://payneinstitute.mines.edu/eog/nighttime-lights/
Administrative boundary		https://www.shengshixian.com

[a]Landsat 8 OLI provides multispectral bands, TIRS provides thermal infrared bands, resampled to 30 m to match the multispectral bands.

τ_{10} represents the atmospheric transmittance for the 10th band, with values for τ_{10} obtained from NASA's official website. L_{10} represents the spectral radiance at the top of the atmosphere for the 10th band, that is, the pixel value after radiometric calibration. T_0 represents the near-surface temperature, which can be substituted with historical weather data.

Urban surfaces are described as mixed pixels comprising buildings and green vegetation, whereas natural surfaces are characterized as mixed pixels consisting of vegetation canopies and bare soil. The surface emissivity for these two classes of mixed pixels can be expressed by the following formula:

$$\begin{cases} \epsilon = P_v R_v \epsilon_v + (1 - P_v)R_m \epsilon_m + d\epsilon \text{ (Urban Surface)} \\ \epsilon = P_v R_v \epsilon_v + (1 - P_v)R_s \epsilon_s + d\epsilon \text{ (natural surfaces)} \end{cases} \quad (6)$$

in which:

$$\begin{cases} R_v = 0.9332 + 0.0585P_v \\ R_m = 0.9332 + 0.1287P_v \\ R_s = 0.9902 + 0.1068P_v \end{cases} \quad (7)$$

$$P_v = \left(\frac{NDVI_i - NDVI_s}{NDVI_v - NDVI_s}\right)^2 \quad (8)$$

$$\begin{cases} d\epsilon = 0.0038P_v \ P_v \leq 0.5 \\ d\epsilon = 0.0038(1 - P_v) \ P_v \leq 0.5 \end{cases} \quad (9)$$

In the equation, P_v represents the vegetation cover percentage, whereas R_v, R_m, and R_s denote the temperature ratios of vegetation, buildings, and bare soil, respectively. ϵ_v, ϵ_m, and ϵ_s are the surface emissivities of the pure pixels of vegetation, buildings, and bare soil, with values of 0.986, 0.970, and 0.972, respectively (Sobrino et al. 2001; Stathopoulou et al. 2007).

3.2 | Remote Sensing Surface Parameter Calculation Method

In this study, six types of remote sensing surface parameters were selected for correlation analysis with the LST. The parameters included the bare soil index (BSI), the modified normalized difference water index (MNDWI), the normalized difference built-up index (NDBI), the normalized difference impervious surface index (NDISI), the NDVI, and the normalized difference water index (NDWI), as depicted in Table 2.

In Table 2, band designations from Landsat 8 are utilized: blue corresponds to Band 2, green corresponds to Band 3, red corresponds to Band 4, NIR (near infrared) corresponds to Band 5, SWIR1 (shortwave infrared 1) corresponds to Band 6, and TIR (thermal infrared) corresponds to the thermal infrared band.

3.3 | Geographically and Temporally Weighted Regression

The geographically and temporally weighted regression (GTWR) model, developed by Huang et al., is an extension of

TABLE 2 | Calculation methods for remote sensing surface parameters.

Surface remote sensing parameters	Calculation formulas
BSI	$\text{BSI} = \dfrac{(\text{SWIR1} + \text{Red}) - (\text{NIR} + \text{Blue})}{(\text{SWIR1} + \text{Red}) + (\text{NIR} + \text{Blue})}$
MNDWI	$\text{MNDVI} = \dfrac{\text{Green} - \text{SWIR1}}{\text{Green} + \text{SWIR1}}$
NDBI	$\text{NDBI} = \dfrac{\text{SWIR1} - \text{NIR}}{\text{SWIR1} + \text{NIR}}$
NDISI	$\text{NDISI} = \dfrac{\text{TIR} - \frac{\text{MNDWI} + \text{NIR} + \text{SWIR1}}{3}}{\text{TIR} + \frac{\text{MNDWI} + \text{NIR} + \text{SWIR1}}{3}}$
NDVI	$\text{NDVI} = \dfrac{\text{NIR} - \text{Red}}{\text{NIR} + \text{Red}}$
NDWI	$\text{NDWI} = \dfrac{\text{NIR} - \text{SWIR1}}{\text{NIR} + \text{SWIR1}}$

the geographically weighted regression (GWR) model (Huang et al. 2010). By incorporating a temporal dimension, the model is able to capture the spatiotemporal dynamics of how explanatory variables influence the dependent variable. The GTWR model provides an accurate description of the spatiotemporal relationships between explanatory variables and the dependent variable. The basic formula for the GTWR model is as follows:

$$Y_i = \beta_0(u_i, v_i, t_i) + \sum_k \beta_k(u_i, v_i, t_i) X_{ik} + \varepsilon_i \qquad (10)$$

in which:

$$\beta_k(u_i, v_i, t_i) = [X^{\mathrm{T}} W(u_i, v_i, t_i) X]^{-1} X^{\mathrm{T}} W(u_i, v_i, t_i) Y \qquad (11)$$

In these equations, (u_i, v_i, t_i) represents the spatiotemporal coordinates of the i-th observation point, Y_i represents the value of the dependent variable for the i-th observation point, and X_{ik} represents the value of the k-th explanatory variable at the i-th observation point. ε_i is the residual term, $\beta_0(u_i, v_i, t_i)$ represents the intercept term for the i-th observation point, $\beta_k(u_i, v_i, t_i)$ represents the coefficient of the k-th explanatory variable for the i-th observation point, $W(u_i, v_i, t_i) = \text{diag}(W_{i1}, W_{i2}, ..., W_{ij})$ is a weight matrix based on spatiotemporal distances, X is the matrix of explanatory variables, and Y is the matrix of dependent variables.

The GTWR model determines the influence weights of other observation points on the current regression observation point by constructing a spatiotemporal weight matrix. Therefore, calculating the spatiotemporal weight matrix is crucial in GTWR model computation. The calculation method of the spatiotemporal weight matrix is as follows:

$$W_{ij} = \exp\left\{ - \frac{\left[(u_i - u_j)^2 + (v_i - v_j)^2\right] + \tau(t_i - t_j)^2}{(h_{\text{ST}})^2} \right\} \qquad (12)$$

In the equation, τ represents the ratio of temporal weights to spatial weights. In this study, τ is set to 1, indicating that time and space are weighted equally. h_{ST} denotes the spatiotemporal bandwidth, indicating the percentage of total data points that are considered neighboring points for the regression analysis. The corrected Akaike information criterion (AICc) is utilized in this study

to determine the optimal h_{ST} of the GTWR model h_{ST}. A smaller value of AICc for the model indicates that the model maintains low complexity while explaining the data. The GTWR model automatically calculates the AICc values corresponding to different h_{ST} values and selects the h_{ST} with the lowest AICc value as a model parameter. The selection of h_{ST} is introduced in the discussion.

4 | Experiments and Analysis of Results

In this study, on the basis of Landsat 8 remotely sensed data, three remote sensing images underwent preprocessing, including geometric correction, radiometric correction, atmospheric correction, and image cropping. The LST and remotely sensed surface parameters were subsequently inverted. Socioeconomic indicators such as NTL and POP were then introduced, all the driving factors were resampled with normalization at a 1000 m × 1000 m resolution to align with the POP, and a spatial autocorrelation test was performed to ensure the significance of the heterogeneity analysis of the SUHI and its driving factors (Ma et al. 2020). Then, the drivers that passed the spatial autocorrelation test were subjected to single-factor GTWR analysis with the LST to analyze the spatial and temporal heterogeneity in their coefficients. Finally, factors that passed the collinearity test were subjected to multifactor GTWR analysis to determine the relationships between the LST and multiple factors. The specific technical flowchart is depicted in Figure 2.

4.1 | Spatial and Temporal Characteristics of the Thermal Environment

The improved single-window algorithm was utilized to obtain the LST for July 31, 2013, September 15, 2018, and August 9, 2022, and the results are presented in Figure 3. The LST distribution map of central Wuhan city in the three periods shows that the SUHI effect prevails in central Wuhan city and is characterized by significantly higher temperatures in the city center than in the surrounding areas. Specifically, heat islands are distributed mainly in the built-up areas on both sides of the Yangtze and Han Rivers, most notably in the east-central part of the study area of the Qingshan Industrial Zone. This may be due to the Wuhan Iron and Steel Company, which contributes to high building density and generates a substantial amount of anthropogenic heat, resulting in elevated temperatures in the area. Conversely, areas comprising water bodies exhibit relatively lower temperatures, which is indicative of a significant cooling effect.

The maximum, minimum, and average temperatures retrieved for the surface are presented in the legends of Figure 3. Throughout the three study periods, the average temperature in central Wuhan exceeded 35°C, with the overall average temperature increasing from 43°C to 45°C. Additionally, both the minimum and maximum temperatures increased by nearly 2°C, which is indicative of a substantial increase in the LST.

4.2 | Spatial and Temporal Characteristics of the Remote Sensing Surface Parameters

Using the remote sensing index calculation method detailed in Table 2, six remote sensing surface parameters, the BSI,
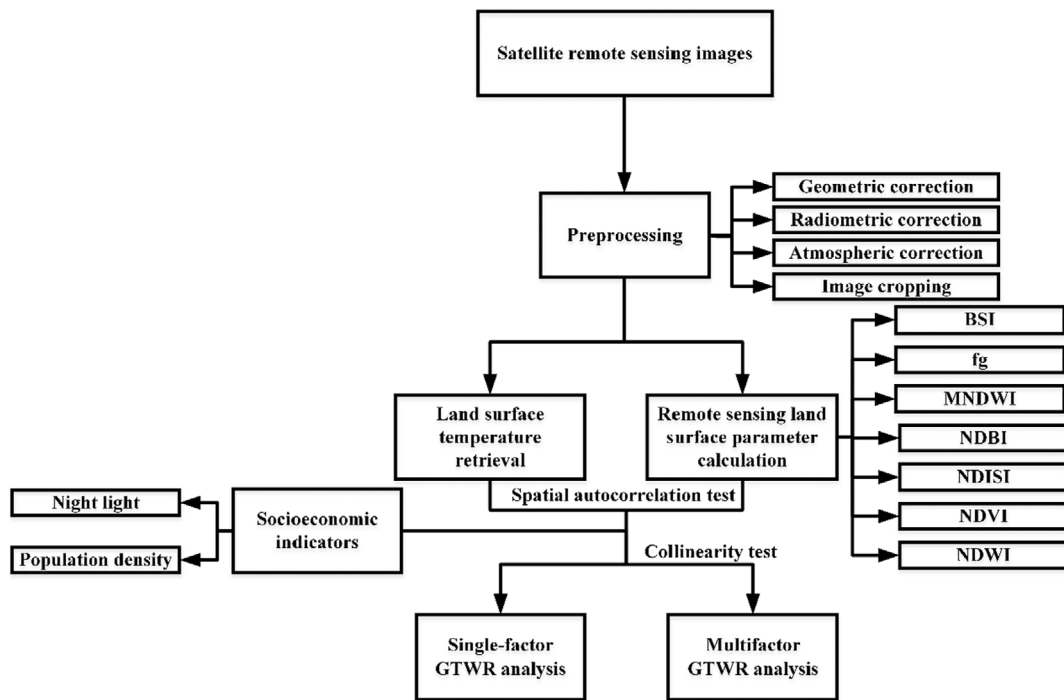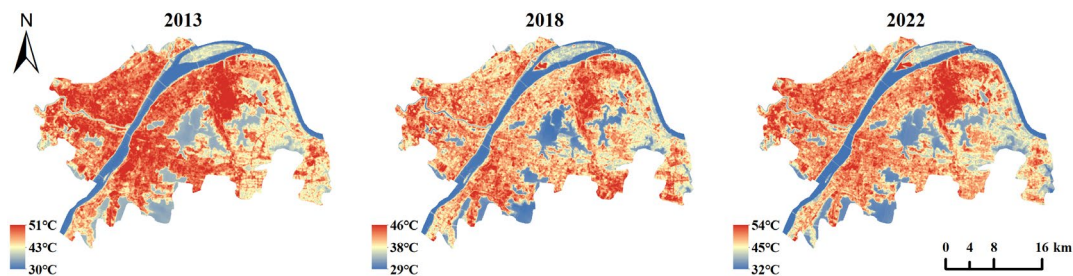
FIGURE 2 | Methodological flowchart.

FIGURE 3 | Spatial distribution of land surface temperature during the three study periods.

MNDWI, NDBI, NDISI, NDVI and NDWI, were acquired, as depicted in Figure 4. Analysis of the distributions of these parameters across the three periods revealed that high values of the BSI, NDBI, and NDISI were predominantly concentrated in the urban center area, whereas high values of the NDVI and NDWI were primarily found in the city's peripheral regions. Conversely, high MNDWI values were distributed mainly in the water body area. Over the three study periods, significant increases in the NDBI and NDISI were observed in the east-central part of the study area, accompanied by a notable decrease in the NDWI, indicating an increase in buildings and impervious surfaces in the east-central part of the Wuhan urban area.

4.3 | Single-Factor Geographically and Temporally Weighted Regression Analysis

To assess the spatial correlation of the variables, Moran's index was selected to evaluate the spatial autocorrelation of several factors. The Moran's index results for all factors passed the statistical significance test, with p values less than 0.01, indicating the presence of highly significant spatial autocorrelation. A total of eight factors, namely the BSI, MNDWI, NDBI, NDISI, NDVI,

NDWI, NTL, and POP, were finally selected for the single-factor GTWR analysis to thoroughly explore the relationships between the LST and individual drivers and to elucidate the specific effects of a single driver on the changes in the LST and its spatiotemporal heterogeneity.

The single-factor GTWR analysis utilized remote sensing surface parameters and socioeconomic indicators in conjunction with the LST, and the results (presented in Table 3) revealed the complex relationships between the LST and drivers in central Wuhan. The BSI, NDBI, NDISI, NLT, and POP were positively correlated with the LST, whereas the MNDWI and NDWI were negatively correlated with the LST. The adjusted coefficient of determination (R^2.adj) reflects the explanatory power of these drivers with respect to the LST, with the NDISI (0.91) showing the strongest correlation and POP (0.37) showing the weakest correlation. Furthermore, NLT, with an R^2.adj of 0.43, displays explanatory power similar to that of the NDVI (0.44), suggesting that NTL is also a robust indicator for analyzing LST changes. The AICc is a criterion for assessing the goodness of fit of statistical models. Among all the factors, the NDISI (-8366) exhibited the best fit with the LST, followed by the MNDWI (-3379) and NDWI (-2726), whereas POP (-1364) demonstrated the poorest
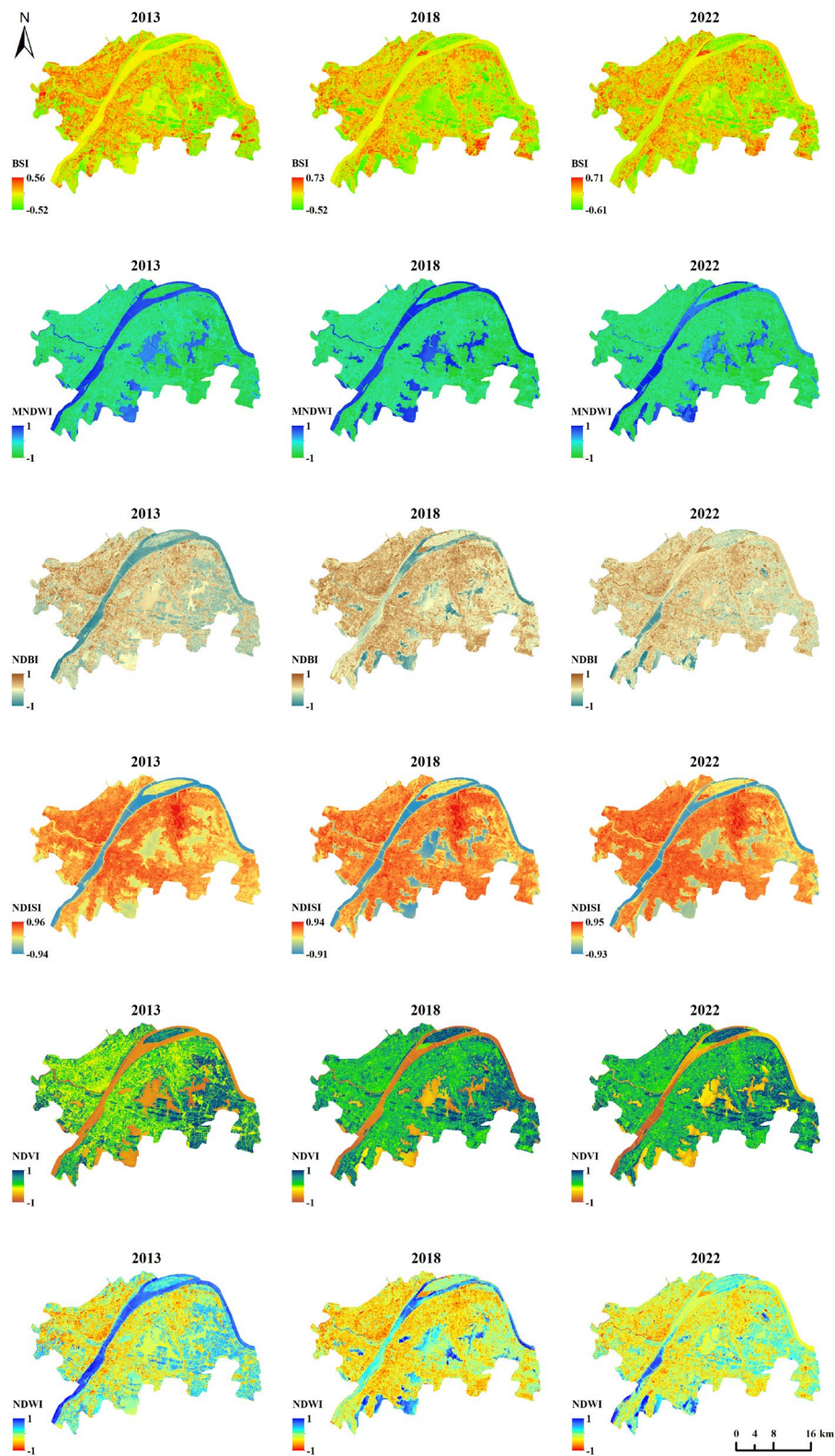
FIGURE 4 | Spatiotemporal distributions of six remote sensing surface parameters across three periods.

fit. In conclusion, the LST in central Wuhan is influenced by a range of environmental and socioeconomic indicators, with the NDISI having the most significant effect on LST, suggesting that urban construction and the increase in impervious surfaces have a significant effect on the increase in LST. The socioeconomic indicators NTL and POP also have a certain positive correlation with the surface urban heat island effect. In contrast, water bodies significantly mitigate the LST.

The distribution of the regression coefficients derived from the GTWR of each driver with the LST is depicted in Figure 5, which demonstrates in detail the spatiotemporal heterogeneity

TABLE 3 | Results of geographically and temporally weighted regression for single factors.

Factor	Average coefficient[a]	R^2.adj	AICc
BSI	0.77	0.50	−2208
MNDWI	−0.65	0.64	−3379
NDBI	1.54	0.57	−2726
NDISI	1.15	0.91	−8366
NDVI	0.44	0.44	−1770
NDWI	−1.54	0.57	−2726
NTL	1.46	0.43	−1718
POP	1.33	0.37	−1364

[a]99.9% of the data passed the significance test with $p < 0.05$.

between each driving factor and the LST. On the basis of the distributions of the regression coefficients, the BSI, NDBI, NDISI, NTL, and POP were mainly positively correlated with the LST, whereas the MNDWI and NDWI were mainly negatively correlated with the LST. Furthermore, the positive and negative correlations between the NDVI and LST vary from region to region; the NDVI and LST are positively correlated in the urban center area and negatively correlated in the peripheral areas.

The LST exhibits variable correlations with the SUHI driving factors in different parts of a city. The positive correlations of the LST with the BSI, NDBI, NDVI, and NTL are more significant in the urban center area than in the peripheral area, whereas the positive correlations with the NDISI are stronger in the peripheral and east-central parts of the study area in the Qingshan Industrial Zone than in the urban center area. The negative correlations of the LST with the MNDWI and NDWI are stronger in the urban center region than in the peripheral area. Analyzing the spatial distribution characteristics of POP reveals that the correlation between POP and the SUHI effect is often greater in sparsely populated areas.

There is a marked time series variation in the correlations between the LST and its drivers. A comparison of the average values of the regression coefficients of the LST and SUHI driving factors over the three study periods revealed that the positive correlations of the LST with the BSI, NDISI, POP, and NTL strengthened, whereas the positive correlations with the NDBI weakened. The negative correlations between the LST and the MNDWI and NDWI weakened. Temporal heterogeneity is more pronounced for the NDBI, NDWI, and POP, with average values of the regression coefficient increments of 0.52, −0.52, and 0.46, respectively. In terms of spatial distribution, the positive correlations of LST with the BSI significantly decreased in the central part of the study area, whereas the high positive correlation with NTL continuously expanded from the two sides of the Yangtze River to the surrounding areas. The positive correlation with the NDISI increased significantly in the east-central part of the study area. Additionally, the positive correlation with the NDBI and the negative correlation with the NDWI were notably strengthened in the southern part of the study area, whereas they declined significantly in the northern part. By analyzing

the spatiotemporal distribution characteristics of the regression coefficients between the LST and SUHI driving factors, the results demonstrate the gradual deepening of urbanization in the central area of the study area and its gradual expansion to the surrounding areas, illustrating the complex spatial and temporal changes in the influence of various SUHI driving factors on the LST.

4.4 | Multifactor Geographically and Temporally Weighted Regression Analysis

To ensure the independence between independent variables, this study employed the variance inflation factor (VIF) to assess the collinearity of the independent variables. The results indicated that the NDBI, MNDWI and NDWI failed the collinearity test, with VIF values of < 5. Consequently, the BSI, NDISI, NDVI, NTL, and POP were selected for multifactor GTWR analysis, and the results are presented in Table 4.

According to the results of the multifactor geographically and temporally weighted regression analysis, the resulting R^2.adj value reached 0.96, and the AICc was −10,994. Compared with the single-factor GTWR model, the multifactor GTWR model has a greater R^2.adj and lower AICc, suggesting that it provides greater explanatory power for LST and more effectively captures the influences of driving factors on LST. The results revealed that the LST is positively correlated with the BSI, NDISI, NTL, NDVI, and POP, and the correlation with the NDISI is the strongest, followed by the BSI, while the correlations with the other variables are comparatively weaker, which is consistent with the findings of the single-factor GTWR analysis. Notably, the highest positive correlation coefficient is associated with the NDISI, highlighting its significant contribution to the SUHI effect through increases in the extent of impervious surfaces. By combining the average correlation coefficients of these drivers, a quantitative model of the relationship between the LST and its drivers can be established, that is, $LST = 1.06NDISI + 0.34BSI + 0.10POP + 0.03NTL + 0.02NDVI − 0.33$.

5 | Discussion

In this study, the GTWR model is used to explore the spatiotemporal heterogeneity between SUHI and their driving factors. In the GTWR model, the spatiotemporal bandwidth h_{ST} significantly influences model performance. A large bandwidth tends to promote global regression, whereas a small bandwidth yields local regression. While a small bandwidth can increase the correlation coefficients, it may also lead to overfitting. To investigate the impact of the spatiotemporal bandwidth h_{ST} on the data fitting efficacy of the GTWR model to select the optimal bandwidth, bandwidth within the range of 0–1 were divided into 10 equal segments in this study, and the AICc was employed as the evaluation metric to determine the optimal bandwidth and their corresponding AICc values at each interval. The AICc's unique penalty mechanism effectively prevents overfitting (Hurvich and Tsai 1989). The results are presented in Figure 6. The experimental results indicate that the AICc value first decreases and then increases as the bandwidth expands, identifying the optimal bandwidth in the second interval (0.1–0.2) with an AICc

value of −10,994. Therefore, the bandwidth of 0.114 in the second interval was selected as the optimal bandwidth in this study.

According to the laws of geography, the relationships among geographical phenomena exhibit universal heterogeneity and gradually weaken with increasing spatiotemporal distance (Tobler 1970, 2004). However, many previous studies overlooked the spatiotemporal heterogeneity between SUHI and their driving factors or oversimplified the concept of distance as merely spatial distance, neglecting temporal distance, potentially leading to inaccurate conclusions (Yang et al. 2020; Zhang, Kafy, et al. 2023). Among the driving factors of the SUHI effect, remote sensing surface parameters are typically constructed based on the spectral reflectance of specific land cover types. These parameters are often associated with one land cover type in high-value areas (the BSI and NDVI) (Wentzel 2002; Tucker 1979) or distinguish between two land cover types using high and low

values (the MNDWI, NDBI, NDISI, and NDWI) (Xu 2006, 2008; Zha et al. 2003; McFeeters 1996). However, in low-value areas or transitional regions between areas of low and high values, the land cover types are usually uncertain, and their contributions to SUHI are unclear. Therefore, exploring the spatiotemporal heterogeneity between SUHI and their driving factors is important for effectively alleviating the aforementioned limitations.

In this study, significant spatiotemporal heterogeneity between SUHI and their driving factors is identified, with the relationship between SUHI and the NDVI displaying the most notable variations. In urban centers, LST is positively correlated with the NDVI, while in other regions, it is negatively correlated. This may be due to the fact that the land cover in the center of Wuhan is mainly composed of water and buildings, while the vegetation coverage is gradually increasing in suburban areas. As the NDVI increases, land cover typically shifts from water
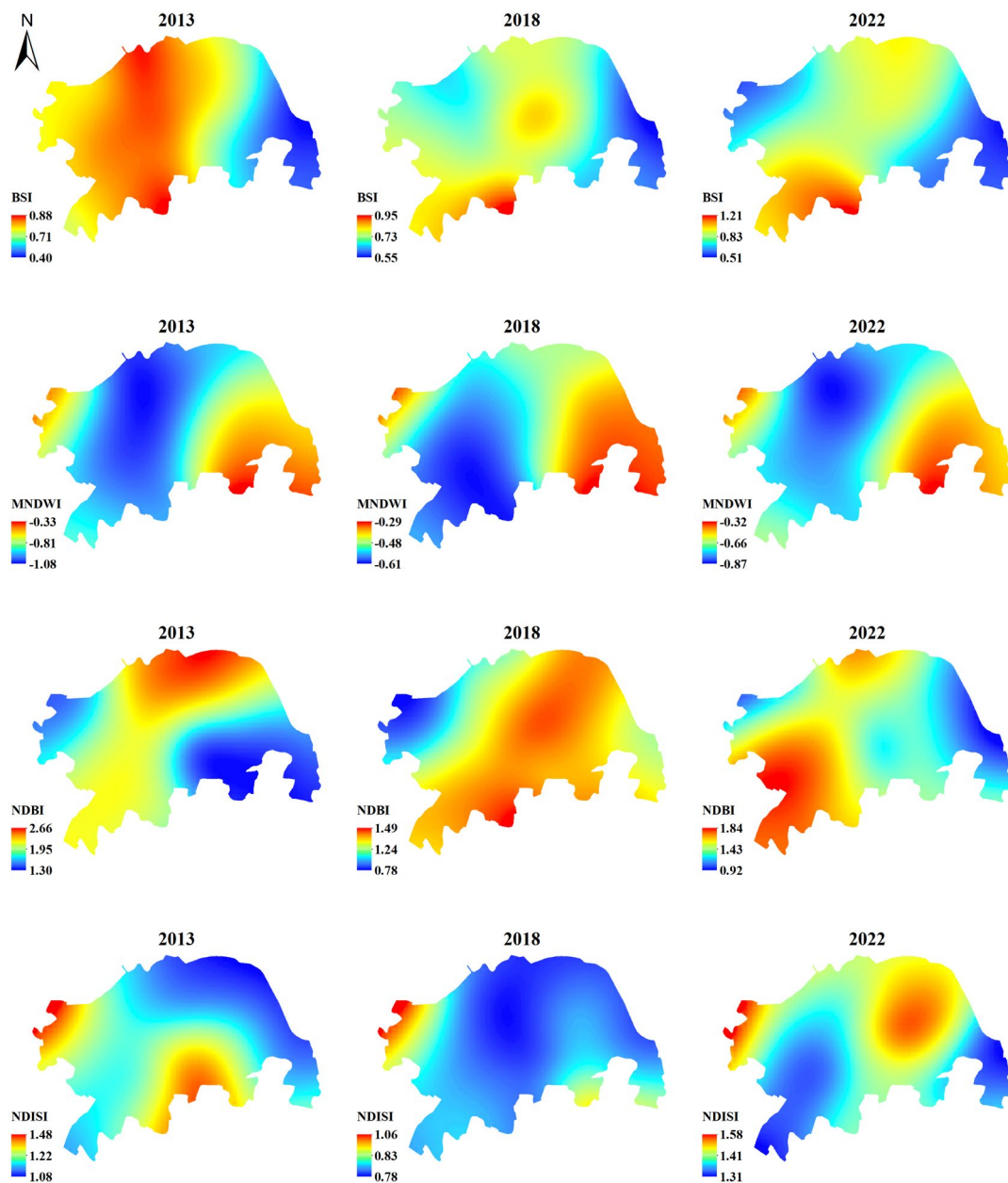

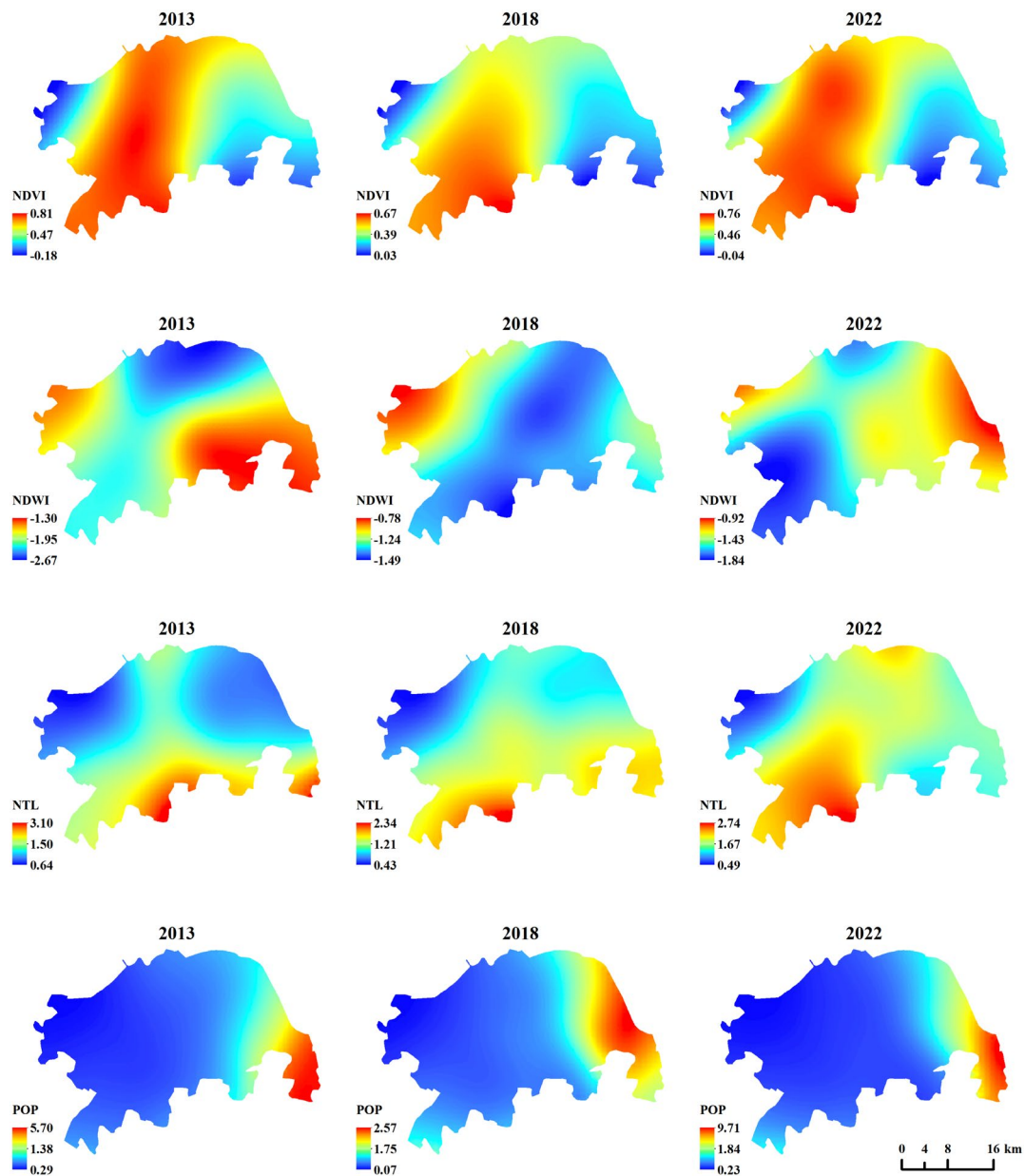**FIGURE 5** | Distribution of regression coefficients for each driving factor.

FIGURE 5 | (Continued)

TABLE 4 | Results of geographically and temporally weighted regression for multiple factors.

Factors	Average coefficient[a]	Intercept	AICc	R^2adj
BSI	0.34	−0.33	−10,994	0.96
NDISI	1.06			
NDVI	0.02			
NTL	0.03			
POP	0.10			

[a]99.99% of the data passed the significance test with $p < 0.05$.

to buildings/bare land and then to vegetation (Shuai et al. 2018). These changes in land cover types affect the LST, corresponding to a cooling–warming–cooling pattern, resulting in positive and negative differences in the correlation between LST and the NDVI in different regions. Therefore, it is crucial to consider their heterogeneity when studying the driving factors of SUHI to avoid drawing biased or completely contradictory conclusions. In this study, other driving factors of SUHI displayed significant spatiotemporal heterogeneity. Exploring the reasons for the heterogeneity of driving factors can improve the accuracy of quantitative analyses of SUHI, with the goal of effectively alleviating the SUHI effect.

6 | Conclusion

In this study, based on Landsat 8 remote sensing data, the single-window algorithm was used to invert the LST. Subsequently, eight drivers—BSI, MNDWI, NDBI, NDISI, NDVI, NDWI, NTL, and POP—were analyzed via single-factor and multifactor GTWR to assess their correlations with LST, explore the
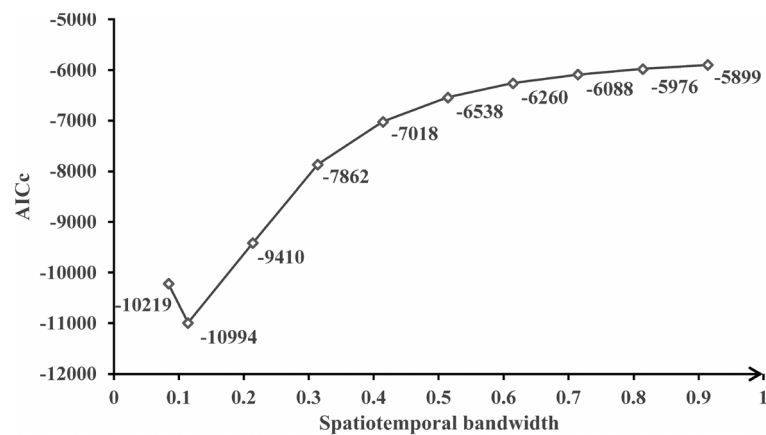
FIGURE 6 | Value of the AICc for different values of spatiotemporal bandwidth.

temporal and spatial heterogeneity of these drivers' influences on the SUHI effect, and synthesize a quantitative relationship between LST and the drivers by determining average correlation coefficients. This comparison elucidated the correlations between the LST and each driver, revealed the diverse spatial and temporal impacts of these drivers on the SUHI effect, and facilitated the construction of a quantitative relationship between the LST and the drivers through the synthesis of average correlation coefficients derived from GTWR analyses.

1. The single-window algorithm is used to invert the LST to obtain a heatmap of the temperature distribution in the center of Wuhan city in 2013, 2018, and 2022, and the experimental results reveal that the SUHI effect prevails in the center of Wuhan city and that the temperature in the center of the city is significantly greater than that in the surrounding suburbs. The heat islands are located mainly in construction areas on both sides of the Yangtze and Han Rivers, most notably in and around the Wuhan Iron and Steel Works in the east-central part of the study area of the Qingshan Industrial Zone, whereas the water body area is relatively cooler and shows a significant cooling effect.

2. Spatial heterogeneity aspects: In the urban center area, the positive correlations of the LST with the BSI, NDBI, NDVI, and NTL are more significant than those in the surrounding areas, the positive correlation with the NDISI is stronger in the surrounding areas and the industrial area than in the urban center area, the negative correlations with the MNDWI and NDWI are more significant than those in the surrounding areas, and the positive correlation between the POP and LST in the eastern part of the study area is stronger than those in other regions.

3. Temporal heterogeneity aspects: Comparing the average values of the regression coefficients of the LST and its drivers during the three study periods, the positive correlations of the LST with the BSI, NDISI, POP, and NTL strengthened, whereas the positive correlations with the NDBI weakened. The negative correlations between the LST and the MNDWI and NDWI weakened. The temporal heterogeneity is more pronounced for the NDBI, NDWI, and POP, with average values of the regression coefficient increments of 0.52, −0.52, and 0.46, respectively.

4. The GTWR analyses of the LST and drivers were synthesized to obtain the average correlation coefficients of each factor, and a quantitative model of the relationship between the LST and drivers was constructed:

$$LST = 1.06NDISI + 0.34BSI + 0.10POP + \ + 0.03NTL + 0.02NDVI - 0.33.$$

In summary, this study reveals the spatiotemporal heterogeneity of LST and its driving factors, emphasizing the importance of spatiotemporal heterogeneity in mitigating the SUHI effect. In the future, it could be possible to integrate resident travel data to assess SUHI effect considering the heat generated by human production activities. In terms of the SUHI driving factors, land use, GDP, and population data could be considered to more comprehensively analyze the SUHI effect.

Conflicts of Interest

The authors declare no conflicts of interest.

Data Availability Statement

All data in support of the findings of this paper are available within the article or as Supporting Information.

References

Chen, T., A. Sun, and R. Niu. 2019. "Effect of Land Cover Fractions on Changes in Surface Urban Heat Islands Using Landsat Time-Series Images." *International Journal of Environmental Research and Public Health* 16, no. 6: 971. https://doi.org/10.3390/ijerph16060971.

Chen, Y., B. Shan, and X. Yu. 2022. "Study on the Spatial Heterogeneity of Urban Heat Islands and Influencing Factors." *Building and Environment* 208: 108604. https://doi.org/10.1016/j.buildenv.2021.108604.

Chu, H. J., B. Huang, and C. Y. Lin. 2015. "Modeling the Spatio-Temporal Heterogeneity in the PM10-PM2. 5 Relationship." *Atmospheric Environment* 102: 176–182. https://doi.org/10.1016/j.atmosenv.2014.11.062.

Deilami, K., M. Kamruzzaman, and Y. Liu. 2018. "Urban Heat Island Effect: A Systematic Review of Spatio-Temporal Factors, Data, Methods, and Mitigation Measures." *International Journal of Applied*

Earth Observation and Geoinformation 67: 30–42. https://doi.org/10.1016/j.jag.2017.12.009.

Feng, X., M. Li, Z. Zhou, F. Li, and Y. Wang. 2023. "Quantifying the Cooling Effect of River and Its Surrounding Land Use on Local Land Surface Temperature: A Case Study of Bahe River in Xi'an, China." *Egyptian Journal of Remote Sensing and Space Sciences* 26, no. 4: 975–988. https://doi.org/10.1016/j.ejrs.2023.11.004.

Fotheringham, A. S., R. Crespo, and J. Yao. 2015. "Geographical and Temporal Weighted Regression (GTWR)." *Geographical Analysis* 47, no. 4: 431–452. https://doi.org/10.1111/gean.12071.

Gao, Y., J. Zhao, and L. Han. 2022. "Exploring the Spatial Heterogeneity of Urban Heat Island Effect and Its Relationship to Block Morphology With the Geographically Weighted Regression Model." *Sustainable Cities and Society* 76: 103431. https://doi.org/10.1016/j.scs.2021.103431.

Ghanbari, R., M. Heidarimozaffar, and A. Soltani. 2023. "Land Surface Temperature Analysis in Densely Populated Zones From the Perspective of Spectral Indices and Urban Morphology." *International Journal of Environmental Science and Technology* 20: 2883–2902. https://doi.org/10.1007/s13762-022-04725-4.

Guha, S., and H. Govil. 2023. "Evaluating the Stability of the Relationship Between Land Surface Temperature and Land Use/Land Cover Indices: A Case Study in Hyderabad City, India." *Geology, Ecology, and Landscapes* 2: 1–13. https://doi.org/10.1080/24749508.2023.2182083.

Gui, X., L. Wang, R. Yao, D. Yu, and C. A. Li. 2019. "Investigating the Urbanization Process and Its Impact on Vegetation Change and Urban Heat Island in Wuhan, China." *Environmental Science and Pollution Research* 26: 30808–30825. https://doi.org/10.1007/s11356-019-06273-w.

Guo, Y., Z. Ren, Y. Dong, et al. 2022. "Strengthening of Surface Urban Heat Island Effect Driven Primarily by Urban Size Under Rapid Urbanization: National Evidence From China." *GIScience & Remote Sensing* 59, no. 1: 2127–2143. https://doi.org/10.21203/rs.3.rs-1295319/v1.

Howard, L. 1833. *The Climate of London*. Vol. 1–3. Harvey and Dorton.

Hu, D. Y., K. Qiao, X. L. Wang, L. Zhao, and G. H. Ji. 2015. "Land Surface Temperature Retrieval From Landsat 8 Thermal Infrared Data Using Mono-Window Algorithm." *National Remote Sensing Bulletin* 19: 964–976. https://doi.org/10.11834/jrs.20155038.

Huang, B., B. Wu, and M. Barry. 2010. "Geographically and Temporally Weighted Regression for Modeling Spatio-Temporal Variation in House Prices." *International Journal of Geographical Information Science* 24, no. 3: 383–401. https://doi.org/10.1080/13658810802672469.

Huang, X., and Y. Wang. 2019. "Investigating the Effects of 3D Urban Morphology on the Surface Urban Heat Island Effect in Urban Functional Zones by Using High-Resolution Remote Sensing Data: A Case Study of Wuhan, Central China." *ISPRS Journal of Photogrammetry and Remote Sensing* 152: 119–131. https://doi.org/10.1016/j.isprsjprs.2019.04.010.

Hurvich, C., and C. Tsai. 1989. "Regression and Time Series Model Selection in Small Samples." *Biometrika* 76, no. 2: 297–307. https://doi.org/10.1093/biomet/76.2.297.

Li, J., R. Sun, T. Liu, W. Xie, and L. Chen. 2021. "Prediction Models of Urban Heat Island Based on Landscape Patterns and Anthropogenic Heat Dynamics." *Landscape Ecology* 36: 1801–1815. https://doi.org/10.1007/s10980-021-01246-2.

Li, X., W. Li, A. Middel, S. L. Harlan, A. J. Brazel, and B. L. Turner Ii. 2016. "Remote Sensing of the Surface Urban Heat Island and Land Architecture in Phoenix, Arizona: Combined Effects of Land Composition and Configuration and Cadastral–Demographic–Economic Factors." *Remote Sensing of Environment* 174: 233–243. https://doi.org/10.1016/j.rse.2015.12.022.

Liao, W., T. Hong, and Y. Heo. 2021. "The Effect of Spatial Heterogeneity in Urban Morphology on Surface Urban Heat Islands." *Energy and Buildings* 244: 111027. https://doi.org/10.1016/j.enbuild.2021.111027.

Liu, W., Q. Meng, M. Allam, L. Zhang, D. Hu, and M. Menenti. 2021. "Driving Factors of Land Surface Temperature in Urban Agglomerations: A Case Study in the Pearl River delta, China." *Remote Sensing* 13, no. 15: 2858. https://doi.org/10.3390/rs13152858.

Ma, X., Y. Ji, Y. Yuan, N. Van Oort, Y. Jin, and S. Hoogendoorn. 2020. "A Comparison in Travel Patterns and Determinants of User Demand Between Docked and Dockless Bike-Sharing Systems Using Multi-Sourced Data." *Transportation Research Part A: Policy and Practice* 139: 148–173. https://doi.org/10.1016/j.tra.2020.06.022.

McFeeters, S. 1996. "The Use of the Normalized Difference Water Index (NDWI) in the Delineation of Open Water Features." *International Journal of Remote Sensing* 17, no. 7: 1425–1432. https://doi.org/10.1080/01431169608948714.

Meng, F., J. Guo, G. Ren, L. Zhang, and R. Zhang. 2020. "Impact of Urban Heat Island on the Variation of Heating Loads in Residential and Office Buildings in Tianjin." *Energy and Buildings* 226: 110357. https://doi.org/10.1016/j.enbuild.2020.110357.

Min, M., L. Chen, X. Duan, Z. Jin, and L. Zhang. 2019. "Spatial Distribution and Driving Force Analysis of Urban Heat Island Effect Based on Raster Data: A Case Study of the Nanjing Metropolitan Area, China." *Sustainable Cities and Society* 50: 101637. https://doi.org/10.1016/j.scs.2019.101637.

Mishra, A., and D. Arya. 2024. "Land Surface Temperature Dynamics During COVID-19 Lockdown in Diverse Climatic and Physiographic Zones—A Study of Indian Mega Cities." *Transactions in GIS* 28, no. 7: 2295–2308. https://doi.org/10.1111/tgis.13237.

Niu, L., Z. F. Zhang, and Z. Peng. 2022. "Driving Factors of Surface Urban Heat Islands in China and Their Spatial Heterogeneity." *China Environmental Science* 42: 945–953. https://doi.org/10.19674/j.cnki.issn1000-6923.20210825.004.

Nowak, D. J., and E. J. Greenfield. 2020. "The Increase of Impervious Cover and Decrease of Tree Cover Within Urban Areas Globally (2012–2017)." *Urban Forestry & Urban Greening* 49: 126638. https://doi.org/10.1016/j.ufug.2020.126638.

Qin, Z., A. Karnieli, and P. Berliner. 2001. "A Mono-Window Algorithm for Retrieving Land Surface Temperature From Landsat TM Data and Its Application to the Israel-Egypt Border Region." *International Journal of Remote Sensing* 22, no. 18: 3719–3746. https://doi.org/10.1080/01431160010006971.

Rao, P. K. 1972. "Remote Sensing of Urban Heat Island From an Environmental Satellite." *Bulletin of the American Meteorological Society* 53: 647–648.

Rees, G., L. Hebryn-Baidy, and V. Belenok. 2024. "Temporal Variations in Land Surface Temperature Within an Urban Ecosystem: A Comprehensive Assessment of Land Use and Land Cover Change in Kharkiv, Ukraine." *Remote Sensing* 16, no. 9: 1637. https://doi.org/10.3390/rs16091637.

Sagris, V., and M. Sepp. 2017. "Landsat-8 TIRS Data for Assessing Urban Heat Island Effect and Its Impact on Human Health." *IEEE Geoscience and Remote Sensing Letters* 14, no. 12: 2385–2389. https://doi.org/10.1109/lgrs.2017.2765703.

Shuai, C., J. Sha, and J. Lin. 2018. "Spatial Difference of the Relationship Between Remote Sensing Index and Land Surface Temperature Under Different Underlying Surfaces." *Journal of Geo-Information Science* 20, no. 11: 1657–1666. https://doi.org/10.12082/dqxxkx.2018.180303.

Si, M., Z. L. Li, B. H. Tang, X. Liu, and F. Nerry. 2023. "Spatial Heterogeneity of Driving Factors-Induced Impacts for Global Long-Term Surface Urban Heat Island." *International Journal of Remote Sensing* 45, no. 19–20: 7139–7159. https://doi.org/10.1080/01431161.2023.2203343.

Sobrino, J. A., N. Raissouni, and Z. L. Li. 2001. "A Comparative Study of Land Surface Emissivity Retrieval From NOAA Data." *Remote Sensing*

of Environment 75, no. 2: 256–266. https://doi.org/10.1016/S0034-4257(00)00171-1.

Soltani, A., and E. Sharifi. 2017. "Daily Variation of Urban Heat Island Effect and Its Correlations to Urban Greenery: A Case Study of Adelaide." *Frontiers of Architectural Research* 6, no. 4: 529–538. https://doi.org/10.1016/j.foar.2017.08.001.

Stathopoulou, M., C. Cartalis, and M. Petrakis. 2007. "Integrating Corine Land Cover Data and Landsat TM for Surface Emissivity Definition: Application to the Urban Area of Athens, Greece." *International Journal of Remote Sensing* 28, no. 15: 3291–3304. https://doi.org/10.1080/01431160600993421.

Templeton, G., and M. Taleghani. 2024. "Micro and Macro Urban Heat Islands in an Industrial City: Bradford, UK." *Nature-Based Solutions* 5: 100124. https://doi.org/10.1016/j.nbsj.2024.100124.

Tobler, W. 1970. "A Computer Movie Simulating Urban Growth in the Detroit Region." *Economic Geography* 46, no. sup1: 234–240. https://doi.org/10.2307/143141.

Tobler, W. 2004. "On the First Law of Geography: A Reply." *Annals of the Association of American Geographers* 94, no. 2: 304–310. https://doi.org/10.1111/j.1467-8306.2004.09402009.x.

Tucker, C. 1979. "Red and Photographic Infrared Linear Combinations for Monitoring Vegetation." *Remote Sensing of Environment* 8, no. 2: 127–150. https://doi.org/10.1016/0034-4257(79)90013-0.

Wang, B., Y. Lei, D. Xue, J. Liu, and C. Wei. 2022. "Elaborating Spatiotemporal Associations Between the Built Environment and Urban Vibrancy: A Case of Guangzhou City, China." *Chinese Geographical Science* 32, no. 3: 480–492. https://doi.org/10.1007/s11769-022-1272-6.

Weng, Q., U. Rajasekar, and X. Hu. 2011. "Modeling Urban Heat Islands and Their Relationship With Impervious Surface and Vegetation Abundance by Using ASTER Images." *IEEE Transactions on Geoscience and Remote Sensing* 49, no. 10: 4080–4089. https://doi.org/10.1109/tgrs.2011.2128874.

Wentzel, K. 2002. "Determination of the Overall Soil erosion Potential in the Nsikazi District (Mpumalanga Province, South Africa) Using Remote Sensing and GIS." *Canadian Journal of Remote Sensing* 28, no. 2: 322–327. https://doi.org/10.5589/m02-013.

Wu, C., F. Gao, X. Ye, and Q. He. 2024. "Unraveling the Impact of Urban Form on Location's Irreplaceability: An Analysis From the Perspective of Spatiotemporal Heterogeneity." *Transactions in GIS* 28: 701–725. https://doi.org/10.1111/tgis.13154.

Wu, Z., Y. Xu, Z. Cao, J. Yang, and H. Zhu. 2021. "Impact of Urban Agglomeration and Physical and Socioeconomic Factors on Surface Urban Heat Islands in the Pearl River Delta Region, China." *IEEE Journal of Selected Topics in Applied Earth Observations and Remote Sensing* 14: 8815–8822. https://doi.org/10.1109/jstars.2021.3108456.

Xu, H. 2006. "Modification of Normalised Difference Water Index (NDWI) to Enhance Open Water Features in Remotely Sensed Imagery." *International Journal of Remote Sensing* 27, no. 14: 3025–3033. https://doi.org/10.1080/01431160600589179.

Xu, H. 2008. "A New Index for Delineating Built-Up Land Features in Satellite Imagery." *International Journal of Remote Sensing* 29, no. 14: 4269–4276. https://doi.org/10.1080/01431160802039957.

Yang, C., F. Yan, X. Lei, et al. 2020. "Investigating Seasonal Effects of Dominant Driving Factors on Urban Land Surface Temperature in a Snow-Climate City in China." *Remote Sensing* 12: 3006. https://doi.org/10.3390/rs12183006.

Zha, Y., J. Gao, and S. Ni. 2003. "Use of Normalized Difference Built-Up Index in Automatically Mapping Urban Areas From TM Imagery." *International Journal of Remote Sensing* 24, no. 3: 583–594. https://doi.org/10.1080/01431160304987.

Zhang, M., A.-A. Kafy, P. Xiao, et al. 2023. "Impact of Urban Expansion on Land Surface Temperature and Carbon Emissions Using Machine Learning Algorithms in Wuhan, China." *Urban Climate* 47: 101347. https://doi.org/10.1016/j.uclim.2022.101347.

Zhang, W., Y. Li, C. Zheng, and Y. Zhu. 2023. "Surface Urban Heat Island Effect and Its Driving Factors for All the Cities in China: Based on a New Batch Processing Method." *Ecological Indicators* 146: 109818. https://doi.org/10.1016/j.ecolind.2022.109818.

Zhao, C., J. Jensen, Q. Weng, and R. Weaver. 2018. "A Geographically Weighted Regression Analysis of the Underlying Factors Related to the Surface Urban Heat Island Phenomenon." *Remote Sensing* 10, no. 9: 1428. https://doi.org/10.3390/rs10091428.

Zhao, J., L. Yu, Y. Xu, et al. 2020. "Exploring Difference in Land Surface Temperature Between the City Centres and Urban Expansion Areas of China's Major Cities." *International Journal of Remote Sensing* 41, no. 23: 8965–8985. https://doi.org/10.1080/01431161.2020.1797216.

Zhao, M., H. Cai, Z. Qiao, and X. Xu. 2016. "Influence of Urban Expansion on the Urban Heat Island Effect in Shanghai." *International Journal of Geographical Information Science* 30, no. 12: 2421–2441. https://doi.org/10.1080/13658816.2016.1178389.

Zhao, M., H. Wang, J. Sun, et al. 2023. "Spatio-Temporal Characteristics of Soil cd Pollution and Its Influencing Factors: A Geographically and Temporally Weighted Regression (GTWR) Method." *Journal of Hazardous Materials* 446: 130613. https://doi.org/10.1016/j.jhazmat.2022.130613.

Zhu, R., É. Guilbert, and M. S. Wong. 2020. "Object-Oriented Tracking of Thematic and Spatial Behaviors of Urban Heat Islands." *Transactions in GIS* 24: 85–103. https://doi.org/10.1111/tgis.12586.